TIME-AVERAGED SPRAY ANALYSIS IN THE NEAR-FIELD REGION USING BROADBAND AND NARROWBAND X-RAY MEASUREMENTS

Danyu Li,[1,] Julie K. Bothell,[1] Timothy B. Morgan,[1] Nathanael Machicoane,[2] Alberto Aliseda,[2] Alan L. Kastengren,[3] & Theodore J. Heindel[1]*

[1]*Center for Multiphase Flow Research and Education, Department of Mechanical Engineering, Iowa State University, USA*

[2]*Department of Mechanical Engineering, University of Washington, USA*

[3]*Advanced Photon Source, Argonne National Laboratory, USA*

*Address all correspondence to: Danyu Li, Center for Multiphase Flow Research and Education, Department of Mechanical Engineering, Iowa State University, Iowa 50011-2161, USA; Tel.: +1 515 294 1423, E-mail: danyuli@iastate.edu

The characterization of a spray in the near-field region is challenging because of its high optical density in this region. X-ray based techniques, with weak scatter and strong penetration properties, can provide better characterization than optical assessment techniques in this region. In this work, the effects of various operating parameters on the optical depth (defined as the accumulated liquid thickness in the beam path times the X-ray attenuation coefficient) and spray profile of an atomizing spray in the near-field region are evaluated based on time-averaged X-ray analysis techniques. Controlling parameters in the spray structure include swirl ratio, liquid phase Reynolds number, and gas phase Reynolds number. Data from the broadband X-ray radiographs obtained using a tube source at Iowa State University and from focused beam measurements at the Advanced Photon Source at Argonne National Laboratory are compared. The X-ray tube source at Iowa State University was operated at two different energy levels, which reveals that the X-ray tube source energy influenced the magnitude of the optical depth but did not change the shape of the distribution. For the no swirl condition, gas flow rate and liquid flow rate had opposite effects on the spray profile, where the spray widens as the gas flow rate increases and narrows as the liquid flow rate increases. As the swirl ratio increases from 0 to 1, the spray widens and then narrows. The critical swirl ratio at which the spray reaches its widest spread differs at different flow conditions.

KEY WORDS: *coaxial atomizer, spray near-field, synchrotron X-rays, tube source X-rays, X-ray radiography*

1. INTRODUCTION

Sprays are an important part of many industrial processes, including energy conversion, propulsion, spray drying, pharmaceutical production, agriculture applications, and additive

manufacturing. Precise control of the spray can effectively improve process efficiency. However, before a spray can be controlled, it must be properly characterized. A spray can be roughly divided into three regions: the near-field, the mid-field, and the far-field. The near-field region, which is the focus of this study, covers the dense spray near the nozzle exit, where primary breakup happens and influences spray formation (Som and Aggarwal, 2010). The near-field region is generally optically dense, increasing the difficulty of characterizing the spray in this region using optical or laser-based techniques (MacPhee et al., 2002). Shadowgraphy, a light refraction-based technique, is commonly used in spray imaging. It captures the interfaces between the liquid and gas; therefore, only the contour of the liquid is shown. But when droplets, ligaments, and other structures overlap, shadowgraphy does not show the change in liquid accumulated thickness. Planar laser-induced fluorescence (PLIF) is another powerful technique for spray visualization. By adding a tracer species in the liquid, it absorbs laser light and then fluoresces at a different wavelength, which can then be used to quantify tracer concentration. However, the attenuation of the laser sheet across the flow field when the spray is optically thick can lead to systematic errors (Mishra, 2014). X-ray-based techniques, with weak scatter and strong penetration, can provide alternative measurements for effective spray characterization (Heindel, 2018).

X-ray radiography is a common X-ray imaging method that produces a shadow-like image of an object where the intensity of the "shadow" is a function of X-ray power and the object's X-ray attenuation (Heindel, 2011). X-rays can be classified according to how the X-rays are produced, and they are generally divided into tube source X-rays and synchrotron source X-rays. Tube source X-ray devices contain two electrodes: the cathode for emitting electrons and the anode as the metal target for the electrons. Broadband tube source X-rays are produced by bombarding the target with high-speed electrons. Synchrotron X-rays are emitted when charged particles, moving at close to the speed of light, interact with bending magnets or undulators.

Synchrotron X-rays, with much higher energy levels and photon flux, can provide more detailed data than tube sources, especially for small-scale objects with low contrast like sprays, because they can provide much higher intensity (flux) levels than tube sources [up to six orders of magnitude higher (Matusik et al., 2018)]. The highly collimated synchrotron X-rays also decrease image distortion caused by cone beams, which are common in tube sources. Because of the higher X-ray flux from synchrotron X-rays, a monochromatic filter can be used in the beam path to produce narrowband X-rays that eliminate beam hardening effects commonly found when using broadband X-rays (Hsieh, 2003). Beam hardening occurs when the X-rays traverse an object, and low-energy X-rays are attenuated more easily than high-energy X-rays. Thus, the attenuation is a function of X-ray wave length (energy), and the total attenuation from a broadband source does not follow a simple exponential decay seen with a monochromatic X-ray (Boas and Fleischmann, 2012). However, the large footprint and high construction and maintenance costs of a synchrotron X-ray facility limit the accessibility of synchrotron X-rays as a regular tool to acquire data. Synchrotron X-rays can only be produced at specialized facilities, such as the Advanced Photon Source (APS) at Argonne National Laboratory. Several investigations using synchrotron X-rays for radiography of sprays have been completed at the APS (Powell et al., 2000; MacPhee et al., 2002; Kastengren et al., 2009, 2014a), where the high-flux X-ray beam provides high spatial and temporal resolution images of the spray. The APS also enables focused beam X-ray measurements by placing a monochromator and focusing mirrors in the beam path while using a PIN photodiode (a diode with a intrinsic semiconductor region between a p-type semiconductor and an n-type semiconductor region) to record the X-ray attenuation in the spray liquid as a function of time along the beam path (Heindel, 2018).

Tube source X-rays typically operate at lower flux levels, limiting penetration and temporal resolution, resulting in lower contrast and quality of the X-ray images. Additionally, monochromatic filters are typically not feasible for tube source X-rays because of the low operating flux. However, the low operating and maintenance costs of tube source X-rays reduce the data acquisition costs, making them easier and more flexible to operate. Tube source X-rays can easily be found in hospitals and universities. Another advantage of tube source X-rays is that they usually provide a larger field of view of the object of interest and can be operated for a long period of time; it can provide a large 2D image over an extended time period. In contrast, synchrotron X-ray sources provide either point measurements using focused-beam radiography or provide an image over a portion of the spray using white-beam imaging (Heindel, 2018). Furthermore, the high energy flux from the synchrotron sources can damage or destroy the object of interest if the exposure time is not limited.

X-ray imaging using a tube source has been used to study multiphase flow with a dense distribution of the dispersed phase (Kingston et al., 2014; Heindel et al., 2008), as well as the near-field region of a spray (Halls et al., 2014b). A comparison of the spray equivalent path length of liquid determined using tube source X-rays and synchrotron X-rays was completed by Halls et al. (2012, 2014a) using an impinging jet spray. In this research, tube source X-rays were used to investigate various spray flow conditions, and selected results were compared to synchrotron X-ray measurements.

The goal of this paper is to reveal the effects of various parameters on the near-field region of a spray from a canonical coaxial two-fluid atomizer. The data obtained from broadband tube source X-ray radiographs are compared to those obtained using focused beam synchrotron radiography. Two spray characteristics that will be reported include optical depth and spray profile. Operating parameters that control the spray structure and are varied in this study include liquid Reynolds number, gas Reynolds number, and swirl ratio. The effect of X-ray tube source energy level in the measurement quality is also studied.

2. EXPERIMENTAL SETUP

In the current research, the broadband X-ray radiographs of the near-field region in a canonical coaxial two-fluid spray were taken using a tube source at Iowa State University. The broadband X-ray radiographs were taken using a LORAD LPX-200 Industrial X-ray source (Heindel et al., 2008). The LPX-200 can generate an X-ray tube potential up to 200 keV, a tube current up to 10 mA, and a maximum allowable power of 900 W. The radiographs were taken at 10 frames per second for 2 minutes (1,200 frames) at each condition, with a field of view of approximately 117×86 mm ($1,388 \times 1,024$ pixels). The exposure time was 20 ms. More details of the X-ray imaging facility at Iowa State University (ISU) can be found elsewhere (Heindel et al., 2008). The focused beam X-ray data were acquired using the 7BM beamline at the Advanced Photon Source of the Argonne National Laboratory. The monochromatic synchrotron X-rays were focused to 5×6 μm full width at half maximum (FWHM) and recorded by a silicon PIN diode at an effective frequency of 270 kHz. Similar techniques were performed by Kastengren et al. (2009, 2012, 2014a,b).

X-ray radiograph quantification is based on the Beer–Lambert law (Pedrotti et al., 2007): if a monochromatic X-ray beam with an intensity of I_0 traverses through a medium, the X-ray energy will be attenuated to I because of absorption, which is a function of the material attenuation coefficient (μ) and the path length (l) through the object, and can be described as follows:

$$I = I_0 \exp(-\mu \cdot l) I = I_0 \exp(-\mu \cdot l) \tag{1}$$

Equation (1) assumes negligible beam scattering, which is an appropriate assumption with X-rays.

For a spray consisting of a distribution of droplets, the path length cannot be determined for individual droplets; instead, the equivalent path length (EPL) is defined as the accumulated length for the liquid phase along the path of the beam and is used to describe the spray structure. Hence, using the Beer–Lambert law, the equivalent path length can be determined as follows:

$$I = I_0 \exp(-\mu \cdot \text{EPL}) = I_0 \exp(-\text{OD}) \tag{2}$$

where I_0 is the intensity without the spray, I is the intensity after passing through the spray, EPL is the equivalent path length for the liquid in the spray, and μ is the attenuation coefficient of the liquid medium through which the beam passes. Note that μ is a function of the material and X-ray energy (wavelength) and is tabulated for monochromatic X-ray sources, like the focused beam radiographic measurements available at the APS. The product of the attenuation coefficient and the equivalent path length is called the optical depth (OD). For the same spray, the averaged EPL from the APS focused beam data and ISU broadband radiographs should be identical:

$$\text{EPL}_{\text{radiograph}} = \frac{\text{OD}_{\text{radiograph}}}{\mu_{\text{radiograph}}} = \frac{\text{OD}_{\text{focused}}}{\mu_{\text{focused}}} = \text{EPL}_{\text{focused}} \tag{3}$$

For narrowband focused beam X-ray data, the attenuation coefficient (μ_{focused}) is a constant, and it is easy to calculate $\text{EPL}_{\text{focused}}$. However, for broadband X-ray radiographs, $\mu_{\text{radiograph}}$ is a complicated function of X-ray wavelength and path length due to beam hardening effects and is difficult to determine directly. Additionally, due to the non-negligible size of the X-ray tube source at ISU, the penumbra, as shown in Fig. 1, complicates the tube source measurements. The penumbra effect happens when the X-ray source cannot be regarded as a point source and is enhanced as the distance between the object and the detector increases. Previous work attempted to account for the effect of beam hardening and penumbra (Li et al., 2018), but the correction lost efficacy when the EPL was small. In the current work, however, a normalized OD was used instead of the EPL to avoid the need for beam hardening and penumbra corrections when describing spray characteristics. Additionally, the results and discussions presented here are based on time-averaged data.

A schematic of the broadband experimental flow loop is shown in Fig. 2. The X-ray tube source, the nozzle, and the imaging system are installed inside a lead-lined X-ray vault. The feed
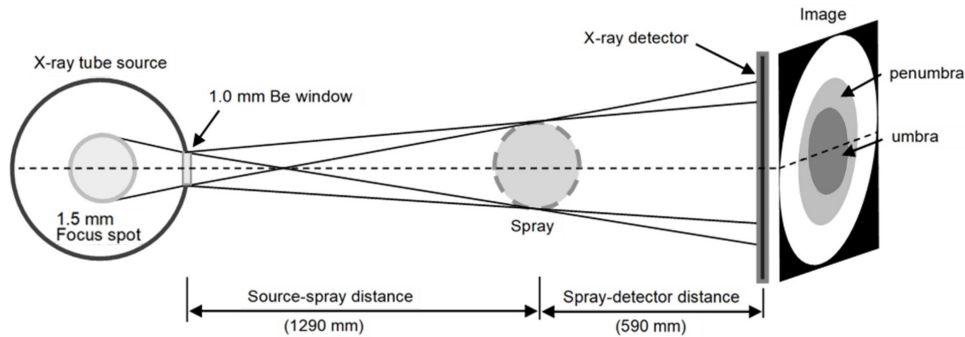
FIG. 1: The penumbra effect in the ISU X-ray facility (not to scale)
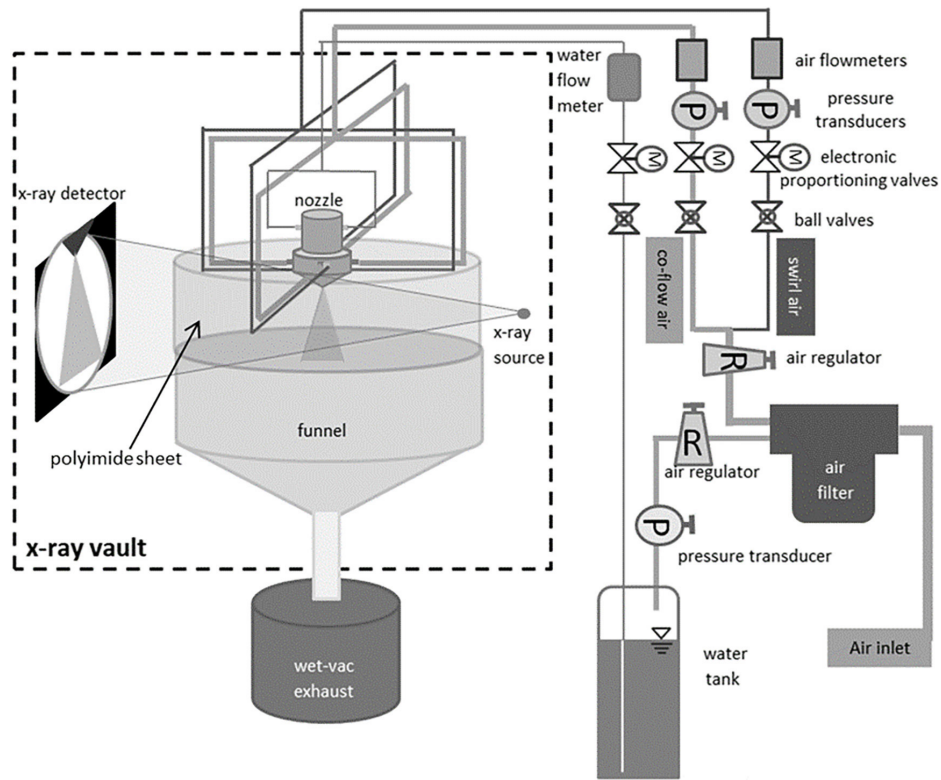
FIG. 2: Schematic of the experimental flow loop at ISU

and collection system, as well as the flow controllers, are located outside the vault. Liquid is forced into the nozzle from both sides. Air is firstly divided into swirl air and co-flow air, and then each air flow line is again subdivided into four branches, each entering the nozzle from four symmetric locations (see Fig. 3). A detailed description of the complete experimental flow loop can be found elsewhere (Li et al., 2018). The flow loop was transported to APS to complete focused-beam measurements using the same system (Bothell et al., 2018, 2019).

The two-fluid coaxial atomizer (University of Washington, 2011) used in this research has been designed to be an open source canonical atomizer that can be reproduced in any laboratory
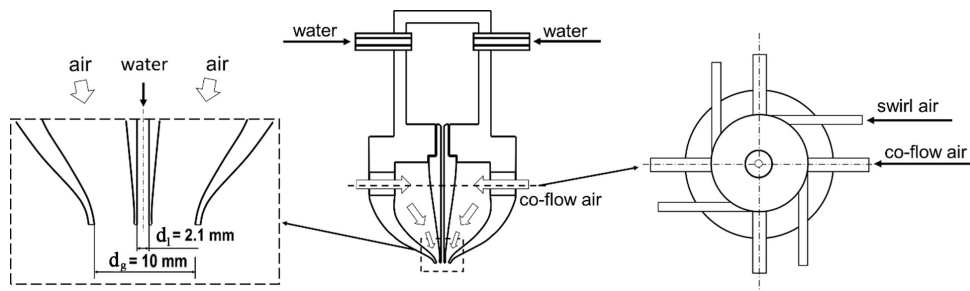
FIG. 3: Schematic representation of the aluminum two-fluid coaxial atomizer

experiment or numerical simulation that aims to compare or validate data against that obtained in this study or others published with this system (Machicoane et al., 2019; Huck et al., 2018). As Fig. 3 suggests, liquid and gas enter the atomizer separately and flow parallel to each other at the nozzle exit. Water enters into the top chamber from both sides, and then flows out through the centrally located liquid needle with an inner diameter $d_l = 2.1$ mm and an outer diameter at the atomizer exit of $D_l = 2.7$ mm. Air is used as the atomizing gas in this study. To investigate the effects of swirl (angular momentum) on the spray, air was divided into two streams, co-flow air and swirl air. Co-flow air enters the gas plenum from four symmetrical inlets that are perpendicular to the water needle centerline. The curved inner wall of the gas plenum turns the air downward to create a coaxial air flow at the nozzle exit, where the inner diameter at the gas exit is $d_g = 10$ mm. When swirl is imparted, a portion of the air stream enters the plenum through four centrosymmetric inlets that are off-axis, creating swirl flow. The concentric liquid and air streams meet and interact at the atomizer exit to create a spray. In this research, the central axis of the atomizer defines the x-axis (vertical axis) and points downward with the origin corresponding to the atomizer exit plane. The y-axis (horizontal axis) is the spray spanwise coordinate. It has an origin corresponding to the liquid needle centerline and is perpendicular to the X-ray beam path direction, which defines the z-axis.

The ratio of swirl air flow rate to co-flow air flow rate is defined as the swirl ratio (SR) to quantify the amount of air entering the gas nozzle through the tangential ports relative to the amount entering perpendicular to the liquid needle.

$$\text{SR} = \frac{\text{swirl air flow rate}}{\text{co-flow air flow rate}} \quad (4)$$

In this study, $0 \leq \text{SR} \leq 1$, and the total gas flow rate remained constant when the swirl ratio was varied. The focus of this study was for $\text{SR} \leq 1$, where the influence of SR was observed, and no data were acquired for $\text{SR} > 1$.

The gas Reynolds number (Re_g) is defined as follows:

$$\text{Re}_g = \frac{U_g d_{\text{eff}}}{\nu_g} = \frac{U_g \sqrt{d_g^2 - D_l^2}}{\nu_g} \quad (5)$$

where U_g is the mean gas velocity at the nozzle exit; ν_g is the kinematic viscosity of air at 25°C; and d_{eff} is the gas effective exit diameter of the air stream at the nozzle exit, defined as the diameter of a circle with the same area as the gas exit area. Two gas Reynolds numbers were investigated: $\text{Re}_g = 21,200$ and $\text{Re}_g = 46,500$.

The liquid phase for the focused beam X-ray data from APS was distilled water. For the ISU broadband X-ray radiographs, 20% by mass potassium iodide (KI) was added to the water as a contrast enhancement agent. The additional KI could increase the surface tension but only by $\sim 2\%$ (Ali and Bilal, 2009), which should not make a significant influence on the spray structure. Also, the work of Halls et al. (2014a) has shown that KI concentration has a linear relationship with the X-ray attenuation coefficient with KI concentrations as high as 20%. Therefore, the 20% KI does not significantly enhance beam hardening. Others have also used KI as a contrast enhancement agent and have shown negligible effects on water density and viscosity, and they observed no change in the flow behavior (Radke et al., 2014; Halls et al., 2014a). The liquid Reynolds number (Re_l) is defined as follows:

$$\text{Re}_l = \frac{U_l d_l}{\nu_l} \quad (6)$$

where U_l is the mean liquid velocity at the nozzle exit; d_l is the inner diameter of the liquid needle (2.1 mm), which is also used as the characteristic length for nondimensionalization; and v_l is the kinematic viscosity of water at 25°C. Note that for the ISU broadband X-ray radiography, although the addition of the KI changed the liquid density slightly (1,196.4 kg/m^3), the liquid Reynolds number mentioned in this paper was still considered as a reference Reynolds number based on pure water at 25°C. Three liquid Reynolds numbers were considered in this study: $Re_l = 1,100, 1,600,$ and 2,200.

Figure 4(a) shows imaging with various KI concentrations (by mass) in the broadband X-ray radiographs for a liquid stream (no gas flow). In these flows, $Re_l = 1,100$ and $Re_g = 0$. The pure water stream is difficult to distinguish from the background. The image contrast improves as the KI concentration increases. Figure 4(b) plots the OD distributions of the liquid streams at $x/d_l = 0.95$ (at 2 mm below the atomizer exit). The maximum optical depth (OD$_{\text{stream}}$) for pure water, 10% KI, 15% KI, and 20% KI is 0.03, 0.15, 0.22, and 0.44, respectively. The increased OD with increasing KI concentration is the result of increased X-ray attenuation (μ), which improves the image contrast.

Peak signal-to-noise ratio (PSNR) for OD is used to evaluate the influence of KI concentration:

$$\text{PSNR} = 10 \cdot \log_{10}\left(\frac{\text{OD}^2_{\text{stream}}}{\text{MSE}_{\text{noise}}}\right) \tag{7}$$

where OD$_{\text{stream}}$ is the maximum OD of the different KI concentrations as mentioned previously; and MSE$_{\text{noise}}$ is the mean square error of OD measured where there is no liquid, representing the noise calculated from a selected region of the background. Note that the MSE$_{\text{noise}}$ is a position-dependent error that is related to the number and position of pixels used in its calculation. Time-dependent noise is minimized by averaging 1,200 radiographic frames. The form of MSE$_{\text{noise}}$ should be the same as OD^2 for comparison:

$$\text{MSE}_{\text{noise}} = \frac{1}{n}\sum_{i=1}^{n}\left[-\log\left(\frac{I_{\text{noise}}}{I_0}\right)\right]^2 \tag{8}$$
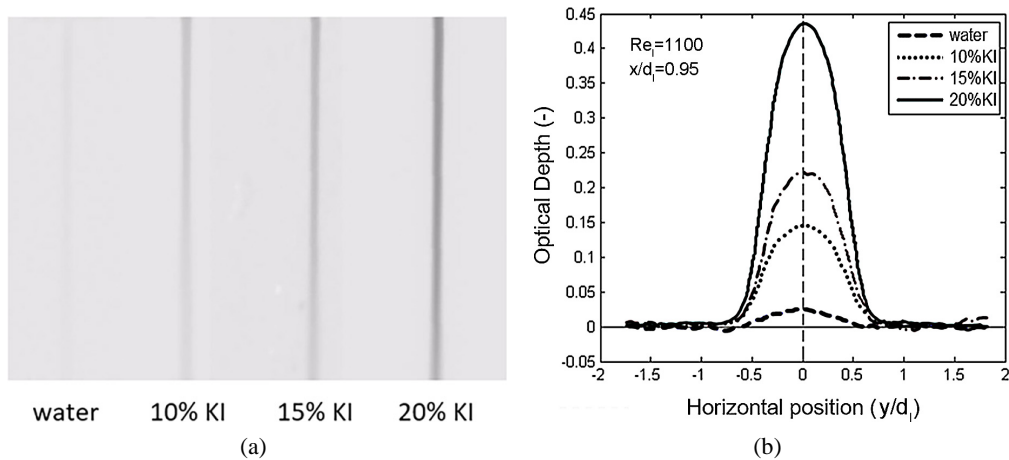
FIG. 4: Liquid streams with changing KI concentration by mass: (a) broadband X-ray radiographs (same colorbar), and (b) optical depth distributions

where n is the number of pixels used to calculate MSE_{noise} ($n = 2,500$); I_0 is the time-averaged background intensity; and I_{noise} is the root mean squared intensity of each pixel used to calculate MSE_{noise}. According to Eqs. (7) and (8), the PSNR for pure water, 10% KI, 15% KI, and 20% KI are 65.4, 97.6, 105.2, and 119.1 dB, respectively. The KI PSNR shows an approximately linear relationship to the KI concentration. Hence, to achieve better contrast, 20% by mass KI was added to the liquid phase for the broadband X-ray radiographs.

3. RESULTS AND DISCUSSION

The following results describe the optical depth maps and profiles of the atomized spray over a range of Re_l, Re_g, and SR. The influence of X-ray tube source energy levels is evaluated. The spray profiles determined from broadband X-ray radiographs with 20% KI added for contrast enhancement are also compared to profiles determined from focused beam measurements of the same atomizing spray using distilled water.

3.1 Optical Depth

The X-ray source operating potential can influence the radiograph intensity, which may affect the data obtained from the image because of beam hardening and the attenuation coefficient, which is a function of wavelength for a polychromatic X-ray beam. In this work, radiographs were taken at two power levels of 100 and 234 W with corresponding potentials summarized in Table 1. Figure 5 shows a comparison of the OD, determined using Eq. (2), with 234 and 100 W power levels at identical spray conditions and axial position. In general, the two plots are both bell-shaped curves, but the magnitudes of the two plots vary greatly because of the different attenuation coefficients caused by the change in X-ray energy. To eliminate the effect of power level, the OD is normalized by the local maximum OD. Note that the local maximum OD is the maximum value at the given axial location and not the maximum for the entire spray.

TABLE 1: Related parameters for different operating potentials

Operating potential	Tube current	Tube potential	Exposure	Frame rate	Frame count
234 W	3.0 mA	78 kV	20 ms	10 FPS	1,200
100 W	2.0 mA	50 kV	20 ms	10 FPS	1,200
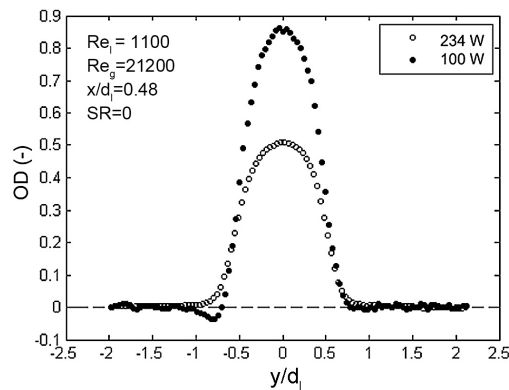
FIG. 5: OD distributions with different X-ray source power levels

Figure 6 shows the normalized OD distributions for the two power levels, where the error bars represent the relative error calculated from the spatially dependent background noise by the 3σ rule (Pukelsheim, 1994). The absolute error in OD is 0.02 for all conditions, and this is normalized by the local maximum OD at the given x-location. At both positions in Fig. 6, the normalized OD distributions are similar regardless of power level. This indicates that the change of X-ray tube source power level does not significantly influence the shape of the OD distribution. Comparing the profiles for the two axial locations of $x/d_l = 1.9$ and 3.33, it is evident that the relative OD error in Fig. 6(b) is larger than in Fig. 6(a). The absolute OD error generally remains unchanged with position, but the maximum OD decreases with increasing x/d_l as the spray spreads out. This leads to an increase in relative error as x/d_l increases. For the same reason, the span of the normalized OD distribution increases from approximately $y/d_l = \pm 0.75$ to $y/d_l = \pm 1.25$ when x/d_l increases from 1.9 to 3.33. The profiles coincide with the radiograph in Fig. 7(b). As the atomized spray disperses, the spray spreads out and dissipates while the image intensity decreases, making it hard to distinguish the spray, which corresponds to the increasing relative error in Fig. 6.

Figure 7(a) shows the magnitude and shape changes of the OD distribution for different axial positions ranging from $x/d_l = 0.48$ to 7.14 when no gas swirl is added (SR = 0). Figure 7(b) is one frame of the corresponding broadband tube source X-ray radiograph. In Fig. 7(a), every distribution shows an approximate Gaussian distribution (Powell et al., 2000; Yue et al., 2001) with a maximum at $y/d_l = 0$ (the central axis). The distributions in the region closest to the nozzle exit (the near-field region) are influenced by a liquid core, showing an obviously flatter top compared to a typical Gaussian distribution. At $x/d_l = 1.9$, the influence of the liquid core becomes negligible. The OD maximum then decreases with increasing axial distance from the atomizer exit. At $x/d_l = 0.48$ ($x = 1$ mm), the maximum OD is 0.87. When x/d_l increases to 4.76 ($x = 15$ mm), the maximum OD decreases to less than 0.1, where the OD distribution flattens out to nearly a straight line. For this no swirl condition, the span of the OD distribution, however, increases slightly with increasing x/d_l, forming a slender spray.

When the swirl ratio increases but Re_g and Re_l remain constant ($\mathrm{Re}_g = 21{,}200$, $\mathrm{Re}_l = 1{,}100$), the OD distribution shows a similar approximate Gaussian feature but the span and magnitude
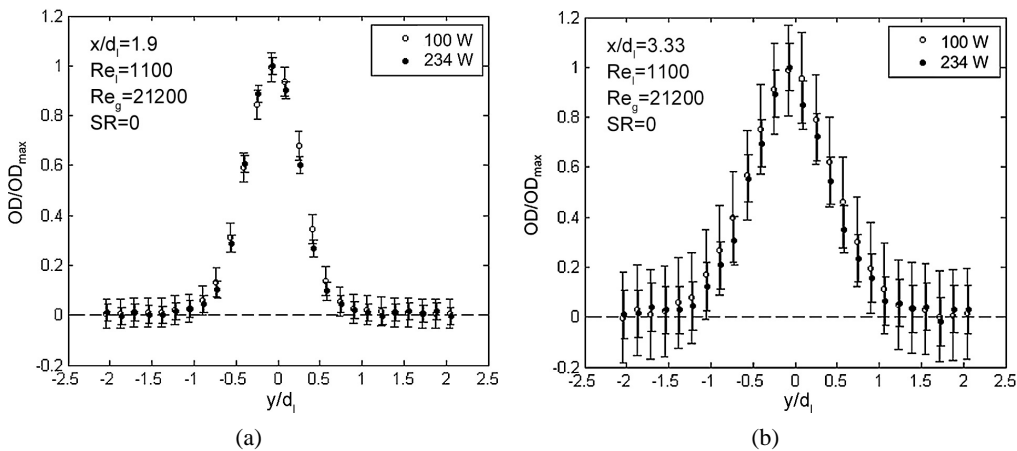
FIG. 6: Normalized OD distributions with different X-ray source power levels at: (a) $x/d_l = 1.9$ ($x = 4$ mm), and (b) $x/d_l = 3.33$ ($x = 7$ mm)
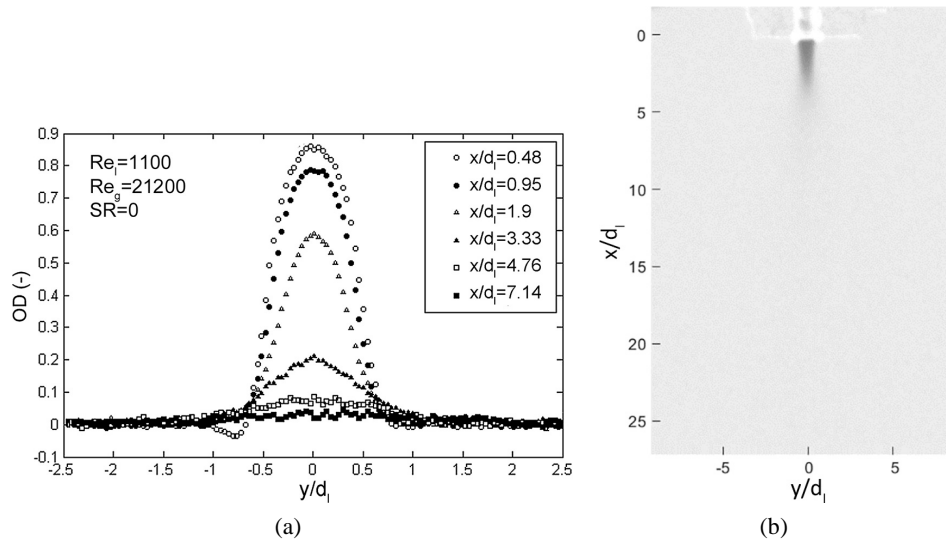
FIG. 7: (a) OD distributions at different axial positions for $Re_l = 1{,}100$, $Re_g = 21{,}200$, and $SR = 0$, with tube power level of 100 W; and (b) corresponding X-ray tube source radiograph

change. At $SR = 0.5$, the OD decreases over a smaller axial distance, and the span increases along the axial direction. When $SR = 1$, the OD profile is similar to that of $SR = 0$. For example, at $x/d_l = 0.48$ [Fig. 8(a)], the normalized OD distributions overlap for $0 \leq SR \leq 1$. This position is close to the atomizer exit, where the spray is not completely developed, and the intact liquid core still has a significant diameter (Bothell et al., 2018). The magnitude of the intact liquid core, common for all swirl ratios, provides the similarity in the OD distributions. At $x/d_l = 1.9$ [Fig. 8(b)], the normalized OD distributions begin to show a trend as a function of swirl ratio. The normalized OD with $SR = 0$ and 0.25 still overlap. However, the normalized OD distributions with $SR = 0.5$, 0.75, and 1 become wider and spread from each other. The distribution with $SR = 0.75$ is the widest, then $SR = 0.5$ and $SR = 1$. At $x/d_l = 3.33$ [Fig. 8(c)], the normalized OD distributions with $SR = 0$ and 0.25 still overlap. The distribution with $SR = 1$ approaches the distributions of $SR = 0$ and 0.25. The distributions with $SR = 0.5$ and 0.75 are much wider. Note there is also more scatter in the data at $x/d_l = 3.33$ because the relative error at this location is larger [see Fig. 6(b)] due to the smaller absolute OD measures (see Fig. 7). This indicates that the spray is more spread out in the radial direction (Hopfinger and Lasheras, 1996). Compared with $SR = 0.5$, when $SR = 1$ the span of the OD distribution decreases. For example, at $x/d_l = 3.33$, the maximum OD are 0.20, 0.09, and 0.43 for $SR = 0$, 0.5, and 1 respectively. This reveals that as SR increases, the spray changes from slender to broad to slender again.

Figure 9 shows a comparison of the normalized OD distributions between broadband and focused beam radiographs. The circles in the plot represent broadband radiograph data (marked as "Radi"), and the triangles represent focused beam data (marked as "FB"). The unfilled symbols represent data at the position $x/d_l = 0.48$, whereas the filled symbols represent $x/d_l = 3.33$. The unfilled circles and triangles overlap, which means that at $x/d_l = 0.48$ where the OD is large, broadband and focused beam measurements are well matched. At this position, the penumbra, beam hardening, and the 20% KI do not show a significant impact on the normalized OD distribution. The filled symbols reveal some differences at $x/d_l = 3.33$. The focused beam OD
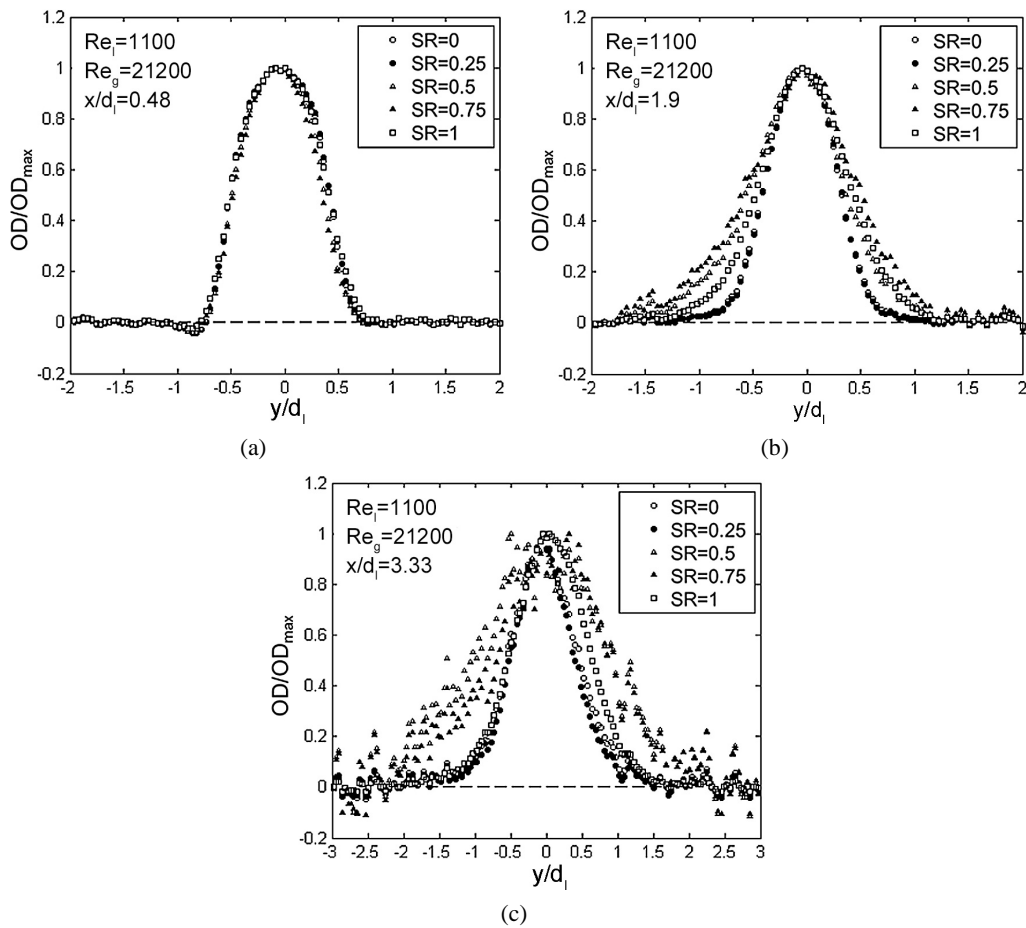
FIG. 8: Normalized OD distributions with various SR: (a) $x/d_l = 0.48$; (b) $x/d_l = 1.9$; and (c) $x/d_l = 3.33$

distribution is narrower than that of the broadband OD. At this axial position, the OD is very small, which enhances the penumbra and beam hardening effects as well as the relative error from the broadband measurements. Hence, the broadband measurements are noisier at this axial position. Furthermore, although the flow loop used in the broadband and focused beam measurements was identical, the exhaust system downstream from the spray was not because of space restrictions at APS. Both exhaust systems provided a slight suction to prevent recirculation. The APS system, however, had a more powerful suction system that could have hindered the spray spreading, making the focused beam profile narrower than the broadband profile, and this was exacerbated further downstream.

3.2 Spray Profile

The edge of the spray at any given axial location is defined as the location where the OD is equal to 1/2 of the maximum OD at that axial location (as shown in Fig. 10), and is used to characterize the spray spatial extent. Because of the limitations in radiography contrast, it is easier and more
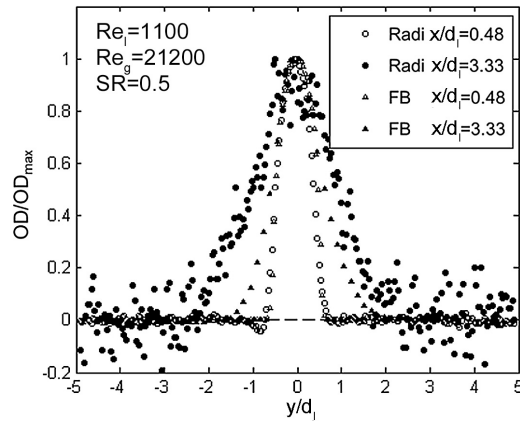
FIG. 9: Comparison of normalized OD distributions between broadband and focused beam radiographs with SR = 0.5

accurate to identify the spray edge using 50% of the local maximum OD, particularly when the OD is small. Figure 10 shows an OD distribution at $x/d_l = 0.95$. For focused beam data, the edge of the spray was defined by interpolating between two data points for which the OD values were closest to the half maximum OD. For broadband radiograph data, of which the interval between data points is very small, the edge of the spray was directly defined by the data point closet to the half maximum OD. The corresponding distances from the spray edges on both sides to the central axis are defined as L_{left} and L_{right}; these two measures are averaged to get a more accurate evaluation of the spray profile, defined as delta:

$$\text{delta} = \frac{1}{2}\left(L_{\text{left}} + L_{\text{right}}\right) \tag{9}$$

The error in delta that resulted from the discreteness of the broadband radiograph data points is ± 0.08 mm, and is assumed to be small when compared to the characteristic length (2.1 mm).
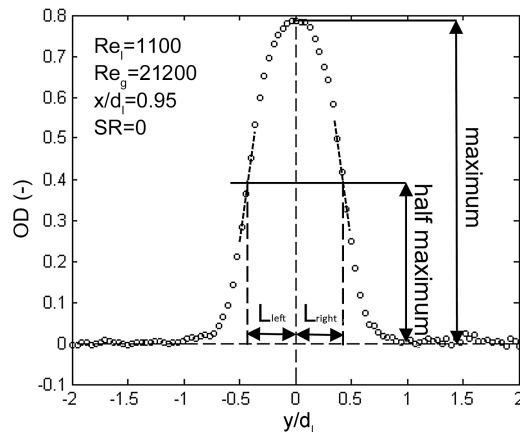
FIG. 10: Defining the edge of the spray at the half maximum OD

The spray profile is determined by plotting the measured delta value at various axial locations. Figure 11 shows the spray profile for two different Re_l and Re_g values for a range of swirl ratios. The atomizer exit plane corresponds to $x/d_l = 0$, but data are available starting at $x/d_l = 0.3$ ($x = 0.63$ mm) because the image at the nozzle exit is distorted due to the image resolution and processing. Note that delta is normalized by d_l. In general, the spray profiles focus near the nozzle exit and then spread out. The focused region correlates with the position where the liquid core (Faeth, 1991) begins to disappear, and the primary atomization has fully occurred (Li et al., 2018). The broadband radiographs have an axial resolution of 0.08 mm, but the data in Fig. 11 shows every fourth data point for better visualization. Figure 11(a) shows the spray profile for $Re_l = 1,100$ and $Re_g = 21,200$. When SR increases from 0 to 0.25, the spray profile remains unchanged. The point of minimum spray width is around $x/d_l = 1.3$. When SR = 0.5, the point of minimum spray width is around $x/d_l = 1.1$, and the spray gets much wider as x/d_l increases. Further increasing SR to 0.75 and then to 1 provides a narrower spray compared to SR = 0.5, and the point of minimum spray width moves downstream to $x/d_l = 1.6$.

Figure 11(b) shows the spray profile for $Re_l = 2,200$ and $Re_g = 46,500$. Compared with Fig. 11(a), Re_g and Re_l are increased. For these conditions, the spray atomization improves and the spray becomes too dilute to be captured by the broadband radiographs, creating large fluctuations in the data when $x/d_l > 3$. At this condition, the profiles for SR = 0, 0.25, 0.5, and 0.75 are similar; the point of minimum spray width corresponds to $x/d_l \approx 1.3$; and delta/$d_l = 0.7$ at $x/d_l = 3$. When SR increases beyond 0.75, the spray widens with the widest profile at SR = 1.
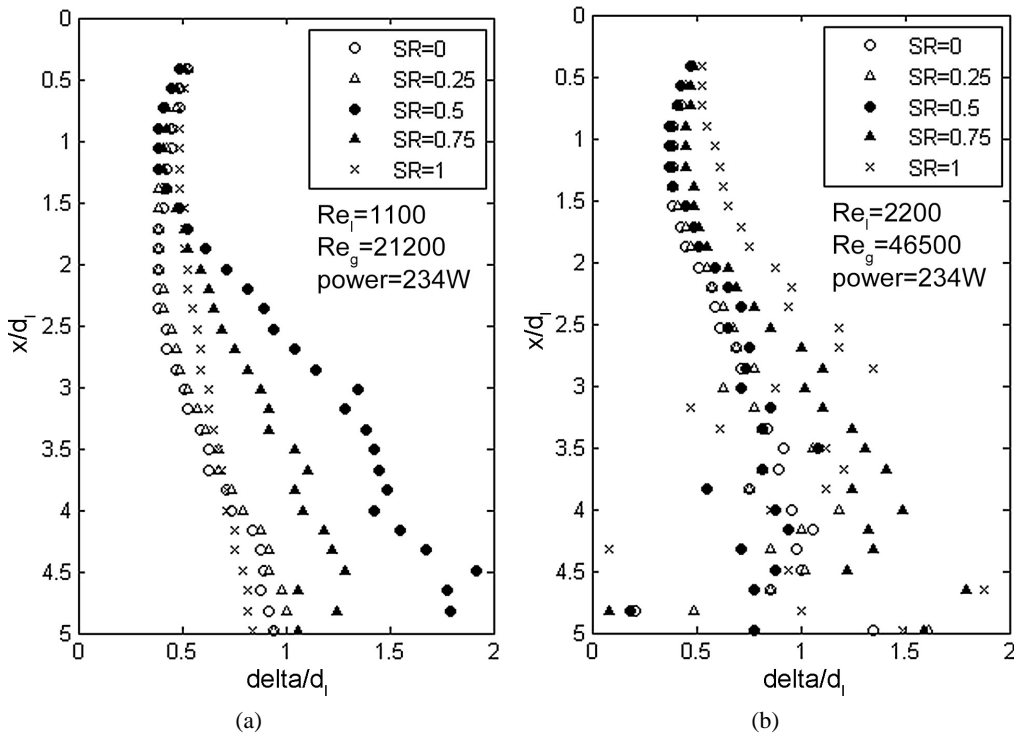
FIG. 11: Spray profiles with various SR at: (a) $Re_l = 1,100$ and $Re_g = 21,200$; and (b) $Re_l = 2,200$ and $Re_g = 46,500$

At SR = 1, the point of minimum spray width seems to move closer to the nozzle exit, showing a shape that gradually widens from top to bottom. In both conditions shown in Fig. 11, a large change in the spray profile happens at certain SRs. For the low gas Reynolds number [Fig. 11(a)], delta sharply increases when SR increases from 0.25 to 0.5. For the high gas Reynolds number, this happens at the maximum SR = 1 [Fig. 11(b)].

In both Figs. 11(a) and 11(b), the spray pattern does not change uniformly with SR. In Fig. 11(a), the plots of SR = 0 and 0.25 almost overlap and suggest a slender spray shape. However, when SR increases to 0.5, the spray reaches its widest. When SR increases to 1, the spray gradually narrows down again. This nonmonotonic change of spray pattern with swirl ratio is caused by the interaction of swirl air and co-flow air. Because the sum of swirl air and co-flow air remained constant, the dominant one could be influenced by Reynolds numbers and could cause the other to weaken, leading to a narrower spray. In Fig. 11(b), the plots of SR = 0, 0.25, 0.5, and 0.75 only have small differences. When SR increases to 1, the spray suddenly widens and reaches its maximum. In both conditions, there is a critical point where the spray suddenly becomes the widest. This point is related to the flow conditions, and before this point, the spray shape does not change significantly with SR. When there is no gas swirl (SR = 0), the effect of Re_g and Re_l on the position of the point of minimum spray width show opposite trends. As shown in Fig. 12(a) for a fixed $Re_l = 2,200$, increasing Re_g from 21,200 to 46,500 causes the point of minimum spray width to move closer to the nozzle exit. The spray also spreads out more as Re_g increases. This is caused by the additional gas momentum enhancing the liquid
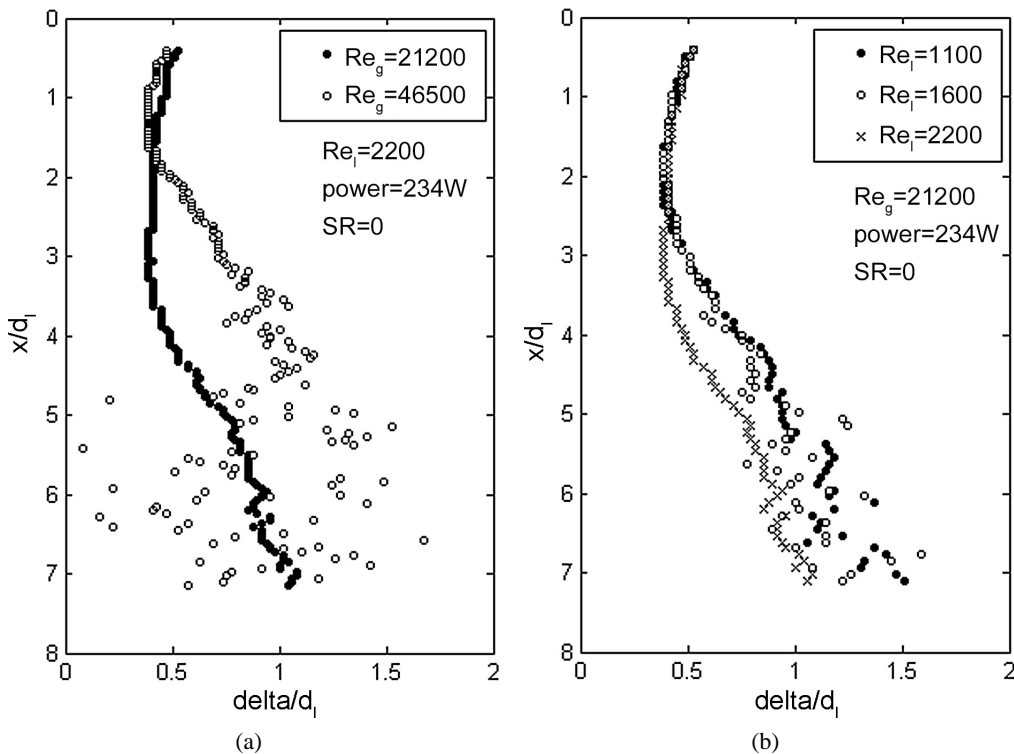
FIG. 12: Spray profiles changing with (a) Re_g; and (b) Re_l while all other conditions are fixed

atomization and mixing, promoting the spreading of the spray. When Re_g is fixed at 21,200 and Re_l increases from 1,100 to 1,600 [Fig. 12(b)], the effects are negligible. However, when Re_l is further increased to 2,200, the point of minimum spray width moves downstream, and the spray elongates. This is caused by the additional mass loading of the liquid, delaying the atomization process and therefore the spreading of the spray. Limited by the image resolution, the spray profiles in the far-field region are hard to analyze and, therefore, not included here. From the near-field results shown here, it appears that Re_g and Re_l also have opposite trends on the spread of the spray in the radial direction. Data from the mid-field region of the spray are needed to confirm this.

Delta from the broadband radiographs is normalized by d_l. As mentioned previously, the error in delta from the broadband radiographs determined by the resolution of the image is fixed at ± 0.08 mm (± 0.04 normalized by d_l). Compared to the characteristic length scale, this error is small; therefore, interpolation was not applied to the broadband radiograph data to determine the edge of the spray. The focused beam data, however, are taken at different sampling intervals, so the normalized error ranges from ± 0.04 to ± 0.23, which requires interpolation to minimize the position error. The broadband radiographs also have a disadvantage because, as the spray disperses (large x/d_l), image contrast decreases and the scatter in the spray profile increases as shown in Figs. 13(a) and 13(b). The spray profiles from broadband radiographs match well with that from the focused beam data at SR = 0 and 0.5, as Figs. 13(a) and 13(b) show. At SR = 1 [Fig. 13(c)], the profile from broadband radiographs is narrower. This is possibly due to the

FIG. 13.

(c)
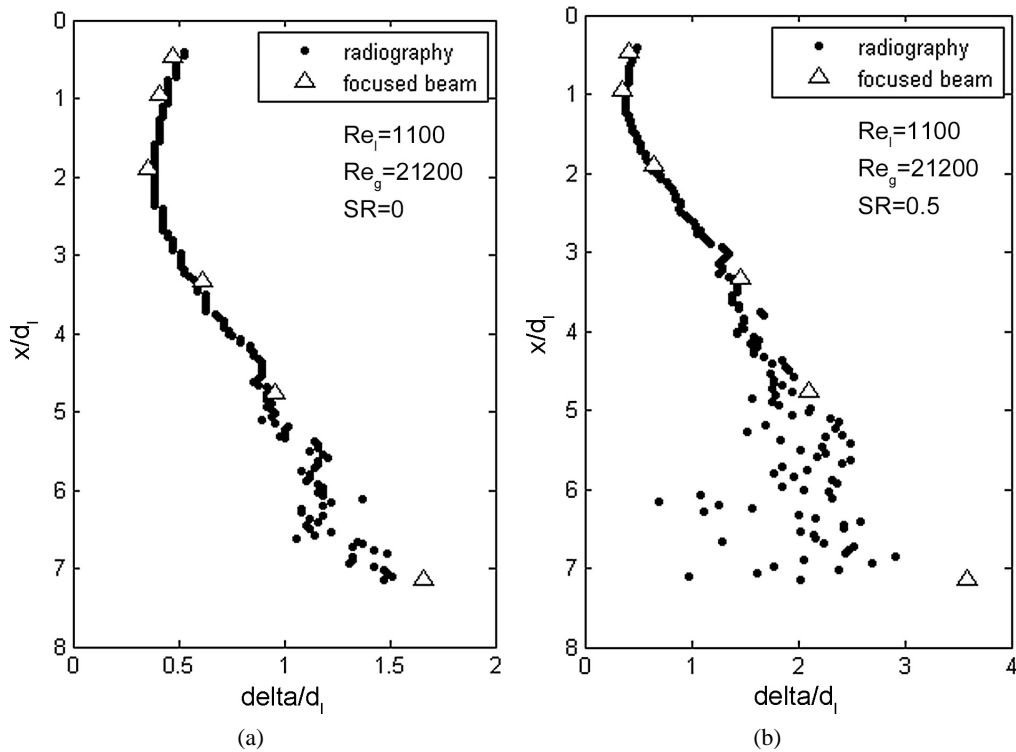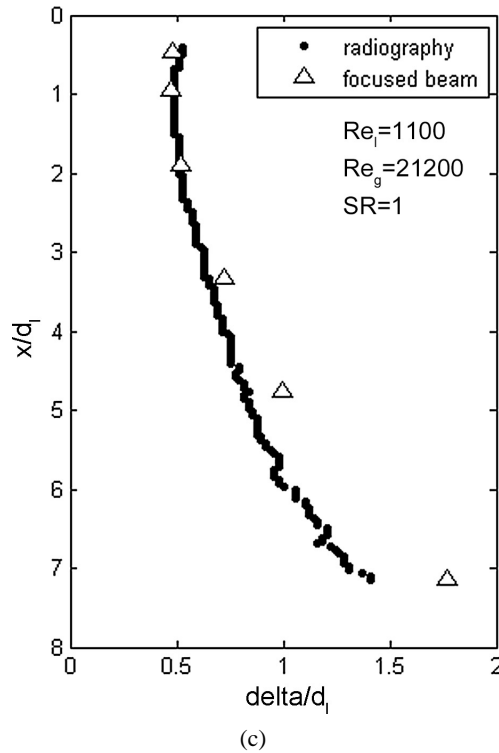
FIG. 13: Comparison of the spray profile between broadband radiographs and focused beam data with (a) SR = 0; (b) SR = 0.5; and (c) SR = 1

atomization enhancement along the radial direction caused by swirl air. Compared with the no swirl condition [Fig. 13(a)], strong swirl air significantly improved spray dispersion along the radial direction and lowered the contrast of the image, causing a narrower spray profile.

4. CONCLUSIONS

The current work evaluated the effect of operating parameters on spray formation from a two-fluid coaxial atomizer in the near-field region. The two metrics of the spray discussed in this work were optical depth (OD) and spray profile. Controlling parameters were the Re_g, Re_l, and swirl ratio. The data obtained from broadband X-ray radiographs using a tube source were compared to synchrotron X-ray focused beam data. Two tube X-ray source energy levels for broadband X-ray radiography were analyzed, and their differences were found to be negligible when the data were normalized properly.

The OD provided an approximate Gaussian distribution across the spray width. The magnitude of the OD decreased uniformly across the spray diameter as the spray developed downstream from the atomizer nozzle. The X-ray tube source energy influenced the magnitude of the OD but did not change the shape of the distribution. Compared to focused beam data, the normalized OD distributions obtained from the broadband radiographs matched well at small x/d_l but deviated at large x/d_l because of the penumbra effect and beam hardening.

The spray profile was defined by the location of the half maximum OD. The swirl ratio influenced the spray profile with trends related to Re_g. At $Re_g = 21{,}200$, the spray widened and then narrowed as SR increased from 0 to 0.5 to 1; the width increased significantly when SR increased from 0.25 to 0.5. At $Re_g = 46{,}500$, the widest spray occurred at the maximum SR studied, SR = 1, and the spray width increased significantly when SR increased from 0.75 to 1. This implied a critical value for SR, related to Reynolds number, above which the spray width increased significantly.

For the no swirl condition, Re_g and Re_l showed opposite effects on the spray profile, where increasing Re_g broadened the spray but increasing Re_l narrowed the spray. Future experiments will further quantify these effects with a narrower interval of the Reynold's number. Compared to focused beam data, the spray profile from the broadband radiographs matched well at SR = 0 and 0.5, but were narrower downstream at SR = 1.

ACKNOWLEDGMENTS

REFERENCES

Ali, K. and Bilal, S., Surface Tensions and Thermodynamic Parameters of Surface Formation of Aqueous Salt Solutions: III. Aqueous Solution of KCl, KBr, and KI, *Colloids Surfaces A: Physicochem. Eng. Aspects*, vol. **337**, nos. 1-3, pp. 194–199, 2009.

Boas, F.E. and Fleischmann, D., CT Artifacts: Causes and Reduction Techniques, *Imaging Med.*, vol. **4**, no. 2, pp. 229–240, 2012.

Bothell, J.K., Li, D., Morgan, T.B., Heindel, T.J., Aliseda, A., Machicoane, N., and Kastengren, A.L., Characterizing the Near-Field Region of a Spray Using White Beam and Focus Beam X-Ray Measurements, *ICLASS 2018, 14th Triennial Int. Conf. on Liquid Atomization and Spray Systems*, Chicago, IL, 2018.

Bothell, J.K., Machicoane, N., Li, D., Morgan, T.B., Aliseda, A., Kastengren, A.L., and Heindel, T.J., Experimental Techniques for the Near-Field Spray Region, *Int. J. Multiphase Flow*, 2019 (in review).

Faeth, G.M., Structure and Atomization Properties of Dense Turbulent Sprays, *Symposium (International) on Combustion*, vol. **23**, no. 1, pp. 1345–1352, 1991.

Halls, B.R., Heindel, T.J., Kastengren, A.L., and Meyer, T.R., Evaluation of X-Ray Sources for Quantitative Two- and Three-Dimensional Imaging of Liquid Mass Distribution in Atomizing Sprays, *Int. J. Multiphase Flow*, vol. **59**, pp. 113–120, 2014a.

Halls, B.R., Heindel, T.J., Meyer, T.R., and Kastengren, A.L., X-Ray Spray Diagnostics: Comparing Sources and Techniques, *50th AIAA Aerospace Sciences Meeting*, AIAA 2012-1055, Nashville, TN, 2012.

Halls, B.R., Morgan, T.B., Heindel, T.J., Meyer, T.R., and Kastengren, A.L., High-Speed Radiographic

Spray Imaging with a Broadband Tube Source, *AIAA Science and Technology Forum and Exposition 2014*, National Harbor, MD, 2014b.

Heindel, T.J., A Review of X-Ray Flow Visualization with Applications to Multiphase Flows, *J. Fluids Eng.*, vol. **133**, no. 7, p. 074001, 2011.

Heindel, T.J., X-Ray Imaging Techniques to Quantify Spray Characteristics in the near Field, *Atomization Sprays*, vol. **28**, no. 11, pp. 1029–1059, 2018.

Heindel, T.J., Gray, J.N., and Jensen, T.C., An X-Ray System for Visualizing Fluid Flows, *Flow Measure. Instrument.*, vol. **19**, no. 2, pp. 67–78, 2008.

Hopfinger, E.J. and Lasheras, J.C., Explosive Breakup of a Liquid Jet by a Swirling Coaxial Gas Jet, *Phys. Fluids*, vol. **8**, no. 7, pp. 1696–1698, 1996.

Hsieh, J., *Computed Tomography: Principles, Design, Artifacts, and Recent Advances*, Bellingham, WA: SPIE Press, 2003.

Huck, P.D., Machicoane, N., Osuna-Orozco, R., and Aliseda, A., Experimental Characterization of a Canonical Two-Fluid Coaxial Atomizer, *ICLASS 2018, 14th Triennial Int. Conf. on Liquid Atomization and Spray Systems*, Chicago, IL, 2018.

Kastengren, A.L. and Powell, C.F., Synchrotron X-Ray Techniques for Fluid Dynamics, *Experiments Fluids*, vol. **55**, no. 3, p. 1686, 2014a.

Kastengren, A.L., Powell, C.F., Arms, D., Dufresne, E.M., Gibson, H., and Wang, J., The 7BM Beamline at the APS: A Facility for Time-Resolved Fluid Dynamics Measurements, *J. Synchrotron Rad.*, vol. **19**, no. 4, pp. 654–657, 2012.

Kastengren, A.L., Powell, C.F., Wang, Y., Im, K.S., and Wang, J., X-Ray Radiography Measurements of Diesel Spray Structure at Engine-Like Ambient Density, *Atomization Sprays*, vol. **19**, no. 11, pp. 1031–1044, 2009.

Kastengren, A.L., Tilocco, F.Z., Duke, D., Powell, C.F., Zhang, X., and Moon, S., Time-Resolved X-Ray Radiography of Sprays from Engine Combustion Network Spray a Diesel Injector, *Atomization Sprays*, vol. **24**, no. 3, pp. 251–272, 2014b.

Kingston, T.A., Morgan, T.B., Geick, T.A., Robinson, T.R., and Heindel, T.J., A Cone-Beam Compensated Back-Projection Algorithm for X-Ray Particle Tracking Velocimetry, *Flow Measure. Instrument.*, vol. **39**, pp. 64–75, 2014.

Li, D., Bothell, J.K., Morgan, T.B., Heindel, T.J., Aliseda, A., Machicoane, N., and Kastengren, A.L., Quantitative Analysis of an Airblast Atomizer in the near-Field Region Using Broadband and Narrowband X-Ray Measurements, *ICLASS 2018, 14th Triennial Int. Conf. on Liquid Atomization and Spray Systems*, Chicago, IL, 2018.

Machicoane, N., Bothell, J.K., Li, D., Morgan, T.B., Heindel, T.J., Kastengren, A.L., and Aliseda, A., Synchrotron Radiography Characterization of the Liquid Core Dynamics in a Canonical Two-Fluid Coaxial Atomizer, *Int. J. Multiphase Flow*, vol. **115**, pp. 1–8, 2019.

MacPhee, A.G., Tate, M.W., Powell, C.F., Yue, Y., Renzi, M.J., Ercan, A., Narayanan, S., Fontes, E., Walther, J., Schaller, J., and Gruner, S.M., X-Ray Imaging of Shock Waves Generated by High-Pressure Fuel Sprays, *Science*, vol. **295**, no. 5558, pp. 1261–1263, 2002.

Matusik, K.E., Sforzo, B.A., Seong, H.J., Duke, D.J., Kastengren, A.L., Ilavsky, J., and Powell, C.F., X-Ray Measurements of Fuel Spray Specific Surface Area and Sauter Mean Diameter for Cavitating and Non-Cavitating Diesel Sprays, *ICLASS 2018, 14th Triennial Int. Conf. on Liquid Atomization and Spray Systems*, Chicago, IL, 2018.

Mishra, D.P., Planar-Laser-Influenced Fluorescence Method, in *Experimental Combustion: An Introduction*, Boca Raton, Florida: CRC Press, pp. 300–306, 2014.

Pedrotti, F.L., Pedrotti, L.S., and Pedrotti, L.M., *Introduction to Optics*, Upper Saddle River, NJ: Pearson

Prentice Hall, 2007.

Powell, C.F., Yue, Y., Poola, R., and Wang, J., Time-Resolved Measurements of Supersonic Fuel Sprays Using Synchrotron X-Rays, *J. Synchrotron Rad.*, vol. **7**, no. 6, pp. 356–360, 2000.

Pukelsheim F., The Three Sigma Rule, *American Statistician*, vol. **48**, no. 2, pp. 88–91, 1994.

Radke, C.D., Heindel, T.J., and Meyer, T.R., Effect of Injector Exit Geometry on Atomization of a Liquid-Liquid Double Swirl Coaxial Injector Using Non-Invasive Laser, Optical, and X-Ray Techniques, *50th AIAA/ASME/SAE/ASEE Joint Propulsion Conf.*, Cleveland, OH, 2014.

Som, S., and Aggarwal, S.K., Effects of Primary Breakup Modelling on Spray and Combustion Characteristics of Compression Ignition Engines, *Combust. Flame*, vol. **157**, no. 6, pp. 1179–1193, 2010.

University of Washington, A Canonical Two-Fluid Coaxial Atomizer, *Multiphase & Cardiovascular Flow Lab*, accessed 2016, from http://depts.washington.edu/fluidlab/nozzle.shtml, 2011.

Yue, Y., Powell, C.F., Poola, R., Wang, J., and Schaller, J.K., Quantitative Measurements of Diesel Fuel Spray Characteristics in the Near-Nozzle Region Using X-Ray Absorption, *Atomization Sprays*, vol. **11**, no. 4, pp. 471–490, 2001.